Analyst

Cite this: *Analyst*, 2012, **137**, 5105

www.rsc.org/analyst

PAPER

Investigation of ion–ion-recombination at atmospheric pressure with a pulsed electron gun

Andre Heptner,*[a] Philipp Cochems,[a] Jens Langejuergen,[a] Frank Gunzer[b] and Stefan Zimmermann[a]

Received 22nd June 2012, Accepted 31st August 2012
DOI: 10.1039/c2an35849b

For future development of simple miniaturized sensors based on pulsed atmospheric pressure ionization as known from ion mobility spectrometry, we investigated the reaction kinetics of ion–ion-recombination to establish selective ion suppression as an easy to apply separation technique for otherwise non-selective ion detectors. Therefore, the recombination rates of different positive ion species, such as protonated water clusters $H^+(H_2O)_n$ (positive reactant ions), acetone, ammonia and dimethyl-methylphosphonate ions, all recombining with negative oxygen clusters $O_2^-(H_2O)_n$ (negative reactant ions) in a field-free reaction region, are measured and compared. For all experiments, we use a drift tube ion mobility spectrometer equipped with a non-radioactive electron gun for pulsed atmospheric pressure ionization of the analytes. Both, ionization and recombination times are controlled by the duty cycle and repetition rate of the electron emission from the electron gun. Thus, it is possible to investigate the ion loss caused by ion–ion-recombination depending on the recombination time defined as the time delay between the end of the electron emission and the ion injection into the drift tube. Furthermore, the effect of the initial total ion density in the reaction region on the ion–ion-recombination rate is investigated by varying the density of the emitted electrons.

Introduction

Ion mobility spectrometry (IMS) is a well-known technique for fast online trace gas detection at atmospheric pressure.[1] Fast response times combined with detection limits in the ppb (parts per billion) and even ppt (parts per trillion) range and good separation power make this technique very interesting for a wide range of applications.[3–7] Typically, IMS is used to detect chemical warfare agents, toxic industrial compounds, explosives and drugs of abuse.[8–13] Due to its fairly simple construction and the beneficial price, IMS is increasingly attractive for other applications, such as food quality monitoring, exhaled breath analysis or the detection of smoldering fires.[14–17] Aiming for higher separation power, as required in most applications, ion specific reaction kinetics – particularly ion generation and ion–ion-recombination – in the reaction region could give additional information besides the ion mobility.[18,19] This is also very interesting for mass spectrometers using atmospheric pressure ionization[20] and IMS-MS tandems.[21] Even more important, selective ion suppression could be an easy to apply separation technique for otherwise non-selective ion detectors. This would allow the development of simple miniaturized sensors based on pulsed atmospheric pressure ionization for the detection of long-lived ion species.

[a]*Institute of Electrical Engineering and Measurement Technology, Department of Sensors and Measurement Technology, Leibniz University Hanover, Appelstr. 9a, Hanover, Germany. E-mail: heptner@geml.uni-hannover.de; Fax: +49 511 7623917; Tel: +49 511 7624222*
[b]*Physics Department, German University in Cairo, Entrance El Tagamoa El Khames, New Cairo City, Cairo, Egypt*

Fundamentals

Ion mobility spectrometry

A drift tube ion mobility spectrometer can be used to analyze chemical substances at atmospheric pressure in air.[1] The IMS can be divided into the ionization region, the drift region and the detection region. In our experiments the ionization source emits electrons with a kinetic energy of a few keV into the ionization region. These electrons mostly ionize nitrogen by electron impact ionization in the ionization region simply due to the high concentration of nitrogen in air. Based on proton transfer reactions, protonated water clusters $H^+(H_2O)_n$, called RIP^+ in the following, are generated.[1] Due to an increasing energy loss of kinetic electron energy attributed to the electron impact, electrons eventually become thermalized so that they can be captured by oxygen. Further chemical gas phase reactions lead to negative oxygen cluster ions $O_2^-(H_2O)_n$, called RIP^- in the following.[1] Depending on their proton and electron affinities, analytes can be ionized by charge transfer reactions from RIP^+ and RIP^- respectively. It is worth mentioning that the exact composition of RIP^+, RIP^- and product ions as present in IMS is hard to measure with *e.g.* mass spectrometry due to possible ion fragmentation. As shown in ref. 2 RIP^+ and RIP^- are most likely $H^+(H_2O)_n$ and $O_2^-(H_2O)_n$.

After ionization the positive and negative ions can be separated by changing the electric potential at the ionization source (injection pulse), leading to a transient electrical field in the reaction region. In the positive mode a positive injection pulse injects the cations into the drift region while the anions are moved to the ionization source where they discharge. In the negative mode the electric parameters are *vice versa* and the generated anions are injected into the drift region. A drift gas is used to purge the drift tube IMS. In the drift tube different ions of one polarity are moved by a homogeneous electric field towards the detection region. During the drift through the drift tube, the ions collide with neutral gas molecules. Due to the ion specific structure and mass, different ion species have different ion mobilities K for a particular drift gas.[4,22] This leads to an ion specific drift velocity v in a given electric field E.

$$v = KE \tag{1}$$

In the detection region, the ions are transferred to a faraday detector which measures the ion current. Depending on the ion mobility, different ion species have different drift times t_d. Thus, ion species are separated based on their ion mobility.

Ion–ion-recombination models and basic considerations

Introducing a time delay between the end of ion generation and ion injection, the following ion loss mechanisms need to be considered.

1. Ions can diffuse to metallic walls, the shutter grid or to the metallic parts of the ionization source, where they discharge. Assuming an inhomogeneous charge distribution in the ionization region this process can be accelerated by coulomb repulsion. In ref. 23 we showed that the ion loss caused by ion diffusion to metallic surfaces is not the dominating ion loss mechanism.

2. Ion–ion-recombination, which is the major reason for ion losses in the ionization region after stopping ion generation and electron emission respectively.[24]

It is important to ensure that there is equilibrium between ion pair generation and all ion loss mechanisms at the end of the ionization process before investigating ion–ion-interactions. In our setup, this equilibrium is achieved after 10 ms of ionization (electron emission time). Moreover, it is important that no electric field separates the anions and cations in the ionization region. Therefore, the ionization region has to be macroscopically field-free.

To explain ion–ion-recombination, we assume that after stopping the ionization only one positive and one negative ion species (for example just positive and negative reactant ions) with concentrations N_+ and N_- exist in the ionization region. Due to Coulomb forces between the cations and anions the ions are mutually attracted. When the distance between a cation and an anion becomes shorter than the critical radius, the probability of the event of ion neutralization is assumed to be 100%.[25]

The ion concentration decay of N_+ or N_- per time due to ion–ion-recombination can be described using a second order differential equation (eqn (2)).[25] The decay depends on the concentrations N_+ and N_- and the recombination coefficient k_r. This recombination coefficient is an ion specific reaction rate that depends on the involved reaction partners, here the positive and negative ions.

$$\frac{dN_+}{dt} = \frac{dN_-}{dt} = -k_r N_+ N_- \tag{2}$$

One electron with a kinetic energy of 8.8 keV – the average kinetic energy of the emitted electrons by the used electron gun – generates approximately 600 anion–cation pairs. Due to the primary excess of electrons from the ionization source the number of anions (601) is slightly higher than the number of cations (600) which will be neglected in the folowing.[26] Thus, the number of cations and anions in the field-free reaction region is assumed to equal $N_+ = N_- = N$. Furthermore, assuming that only singly ionized ions exist in the ion cloud,[25] the ion concentrations N_+ and N_- can be replaced by the measurable charges of the cations $|Q_+|$ and anions $|Q_-|$ and eqn (2) can be rewritten as follows.

$$\frac{d|Q|}{dt} = -k_r |Q|^2 \tag{3}$$

A solution[19] for eqn (3) is shown in eqn (4). The charge $|Q(t_{rec})| = |Q_+(t_{rec})| = |Q_-(t_{rec})|$ depends on the initial charge $|Q_0| = |Q_{0,+}| = |Q_{0,-}| = |Q(t_{rec} = 0)|$, the recombination time t_{rec} and the ion specific recombination coefficient k_r.

$$|Q(t_{rec})|^{-1} = \frac{1}{|Q_0|} + k_r t_{rec} \tag{4}$$

The benefit of this mathematical representation is that the recombination coefficient k_r is equal to the slope of the $|Q(t_{rec})|^{-1}$-curve, which is simply a straight line according to eqn (4). Moreover, the reciprocal value of $|Q_0|$ is the intercept with the y-axis.

Experimental section

For investigating the ion–ion-recombination we used a drift tube IMS coupled to a pulsed, non-radioactive electron gun[27] for all measurements. The used drift tube IMS has an inner diameter of 15.2 mm, a 2.5 mm long ionization region and a 70.5 mm long drift region. We used dry clean air as the drift gas whereby the concentration of water vapor was kept constant at 8.18 ppm (dew point of −62 °C).

For the ionization a non-radioactive pulsed electron gun from Optimare Analytik GmbH & Co. KG is used. This electron gun emits electrons with a simulated average kinetic energy of 8.8 keV through a silicon nitride membrane from vacuum into atmospheric pressure.[28] The silicon nitride membrane is 1 mm^2 with a thickness of 300 nm.[29] Simulations were used to estimate the maximum electron penetration depth in air, which was found to be about 2 mm, leading to an estimated ionization volume of 40 mm^3 in air. As mentioned above, the emission time t_{em} during which the electron gun emits electrons is set to 10 ms. These electrons ionize the neutral gas mixture (Fig. 1). During the emission time t_{em} and the recombination time t_{rec} the ionization region is macroscopically field-free. This is not possible when using a Bradbury–Nielsen ion shutter. A detailed description of the Bradbury–Nielsen ion shutter principle is given in ref. 30 Thus, we inject the ions with a transient electrical field. At all other times the electric potential of the ionization source equals the potential of the injection grid (Fig. 1–3).

The recombination time t_{rec} between the end of t_{em} and the injection pulse is varied from 0 to 10.05 ms in 150 µs steps. After

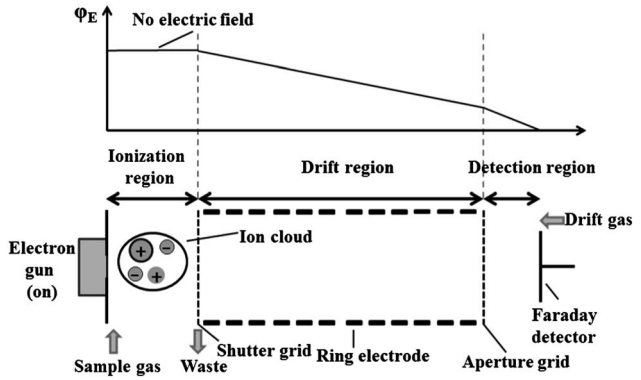

Fig. 1 Schematic of the drift tube IMS equipped with a non-radioactive pulsed electron gun as the ionization source. The electron gun emits electrons with an average kinetic energy of 8.8 keV for 10 ms to ionize the gas mixture by atmospheric pressure ionization. Additionally, the potential distribution during t_{em}.

the electron emission stops the generated total ion concentration in the ionization region starts to decrease (Fig. 2). At the end of t_{rec} the ion density in the ionization region is decreased (Fig. 3).

Subsequently the remaining ions are separated by the injection pulse and all ions of one polarity are accelerated to the faraday detector while the others discharge at the conducting ionization source (see Fig. 4). Separating the cations from the anions also defines the end of ion–ion-recombination.

In all measurements the ion current is detected within a drift time frame from $t_d = 2$ ms to $t_d = 32$ ms with a temporal resolution of 15 μs. Fig. 5 shows the timing diagram including the electron emission t_{em}, the time t_{rec} between the end of the ionization and the ion injection, the injection pulse width t_{inj} and the drift time t_d.

The operating parameters of the electron gun and the drift tube IMS are listed in Table 1.

For sample gas generation – dry clean air containing the analytes – we use a permeation oven that is operated with a constant carrier gas flow at a constant temperature. All chemicals are from Sigma Aldrich (DMMP: D169102, acetone: 650501, ammonia carbonate: A9516-100G). To control the analyte concentration we mix up to 550 ml min^{-1} of the sample gas with 2000 ml min^{-1} dry clean air. The analyte concentrations in the sample gas are calculated from the loss of weight of the permeation tubes per time divided by the flow rate and mixing ratio. The concentrations are not measured by a reference system.

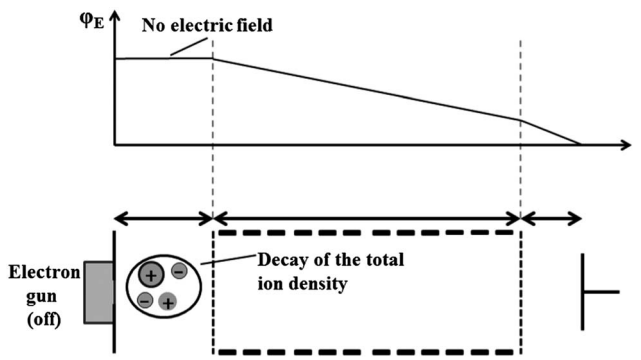

Fig. 2 The electron gun is turned off, the electron emission stops and the generated ions start to decrease in the ionization region. Additionally, the potential distribution during t_{rec}.

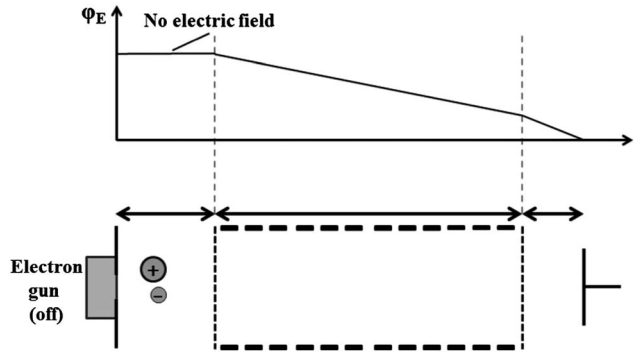

Fig. 3 After a certain recombination time, all short-lived ion species recombine and only the long-lived ion species are still present in the ionization region. Additionally, the potential distribution during t_{rec}.

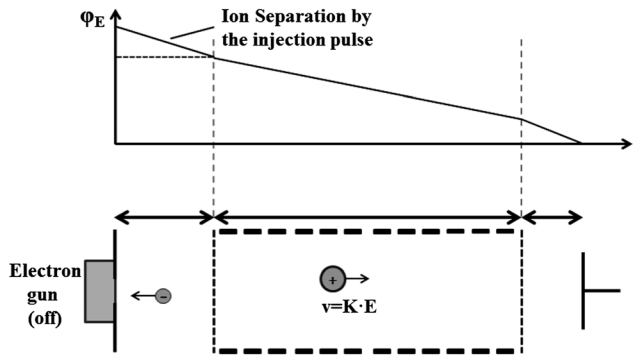

Fig. 4 At a defined recombination time t_{rec} the remaining cations and anions are separated by the injection pulse. The injection pulse leads to ion separation in the ionization region.

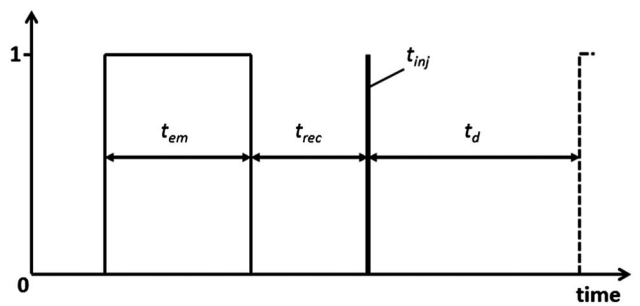

Fig. 5 Timing diagram: emission time $t_{em} = 10$ ms, variable recombination time $t_{rec} = 0…10.05$ ms, injection time $t_{inj} = 350$ μs and drift time $t_d = 30$ ms.

Results and discussion

Measurements showed that an electron emission time t_{em} of 10 ms is sufficient to reach the mentioned equilibrium between ion generation and ion losses giving a constant ion density in the ionization region with an equal number of anions and cations even for longer ionization times. Thus, after stopping the

Table 1 Operating parameters of the IMS and electron gun

Parameter (IMS)	Value
Temperature	20 °C
Drift tube pressure	1018 mbar
Dew point (drift and sample gas)	−62 °C
Drift gas	500 ml min^{-1}
Sample gas	5 ml min^{-1}
Electric drift field	285 V cm^{-1}
Injection field	1750 V cm^{-1}
Injection time t_{inj}	350 µs
Injection frequency	16 Hz
Parameter (electron gun)	Value
Average electron energy	8.8 keV
Emission time t_{em}	10 ms
Recombination time t_{rec}	0…10.05 ms
Transmitted electron current	10…100 pA

electron emission the process of ion–ion-interactions in the field-free ionization region can be investigated.

In Fig. 6 the positive ion mobility spectra of dry clean air at different recombination times t_{rec} are shown. The dominant peak at $t_d = 12.19$ ms is the positive reactant ion peak (RIP^+) with $K = 2.21$ cm^2 V^{-1} s^{-1}. The amplitude of the RIP^+ decreases with increasing t_{rec}, while the peak at $t_d = 14$ ms – an unidentified impurity – decreases with a significantly lower rate.

We also measured the ion mobility spectra of dry clean air at different recombination times in the negative IMS mode, see Fig. 7. Here, the dominant ion species is the negative reactant ion at $t_d = 11.54$ ms which also decreases with increasing t_{rec}.

As mentioned above, ion–ion-recombination is the dominant ion loss mechanism in the ionization region after stopping the electron emission. In order to apply the theory of ion–ion-recombination to our measurements, it is necessary to know the total charge in the ionization region which can be derived from the detected charge $|Q'|$ at the faraday detector. From ref. 23 it is known that $|Q'| = ½|Q|$. Therefore, the ion current at the detector is integrated over the drift time for each ion mobility spectrum according to eqn (5) giving the time dependent total charge in the ionization region $|Q(t_{rec})|$.

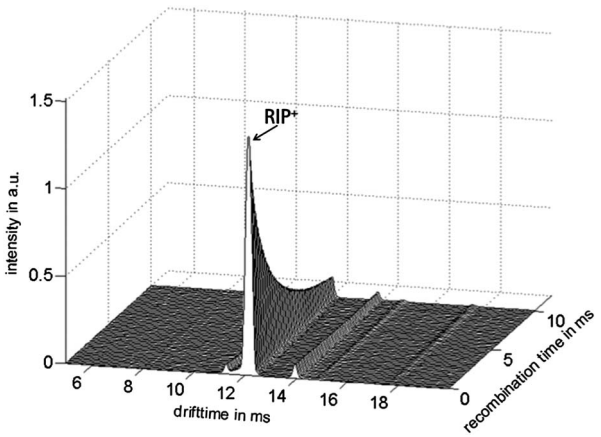

Fig. 6 Positive ion mobility spectra of dry clean air at different recombination times. Drift time (*x*-axis), recombination time (*y*-axis) and intensity (*z*-axis). The dominant ion species is the positive reactant ion at $t_d = 12.19$ ms.

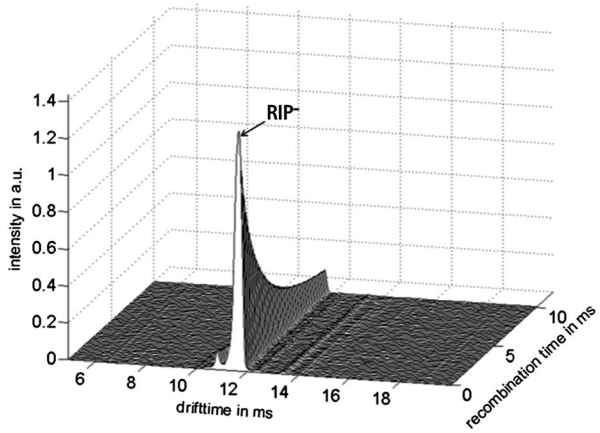

Fig. 7 Negative ion mobility spectra of dry clean air at different recombination times. Drift time (*x*-axis), recombination time (*y*-axis) and intensity (*z*-axis). The dominant ion species is the negative reactant ion at $t_d = 11.54$ ms.

$$|Q| = 2\int_{2ms}^{32ms} I\,dt_d \qquad (5)$$

In Fig. 8 the reciprocal total charge at the faraday detector $|Q(t_{rec})|^{-1}$ for the positive and negative modes are plotted. As in theory, $|Q(t_{rec})|^{-1}$ is proportional to the recombination time t_{rec}, where the recombination coefficient k_r is the proportionality constant and slope respectively, and $|Q_0|$ the intercept with the *y*-axis. Furthermore, the measured positive and negative charges $|Q(t_{rec})|$ are almost equal for all recombination times, and the measured decay curves perfectly match the mathematical description according to eqn (4). Thus, the recombination coefficients k_r of positive and negative reactant ions are equal and calculated to 2.1×10^{16} 1 C^{-1} s^{-1} – a sound result, since positive reactant ions can only recombine with negative reactant ions in this experiment. Additionally, this confirms the assumption that the amount of positive ions equals the amount of negative ions in the ionization region for every recombination time and $N_+ = N_-$ is valid. Due to the decreasing signal to noise ratio with increasing t_{rec}, the variation between the measurement data and the theoretical progression becomes higher.

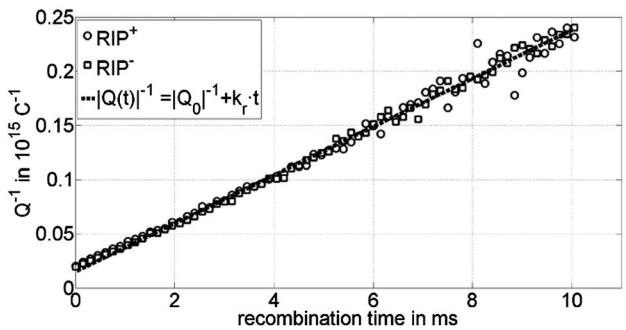

Fig. 8 $|Q(t_{rec})|^{-1}$ curves of the measured positive (empty circles) and negative (empty squares) total charge at the faraday detector and theoretical curve (black dashed curve) considering ion–ion-recombination as the major effect on the ion loss according to eqn (4).

To further investigate the recombination coefficient k_r, decay curves of the positive reactant ion peak were measured for different initial total charges $|Q_0|$ that can be varied by simply varying the electron emission current of the electron gun. Fig. 9 shows the measured $|Q(t_{rec})|^{-1}$-curves. According to eqn (4), a change in $|Q_0|$ should only lead to different intercepts with the y-axis. However, it can be seen in Fig. 9, that varying $|Q_0|$ leads to different slopes and recombination coefficients respectively. This can be explained by a higher diffusion constant D for ions with higher K as described by the Nernst–Einstein-equation (eqn (6)).[31]

$$K = \frac{eD}{kT} \tag{6}$$

According to eqn (7) in ref. 32, the measured recombination coefficient k_r depends on a constant recombination coefficient k_{rt} plus a correction term which depends on the initial charge Q_0 and a constant factor C. Hence, the correction term becomes smaller for lower initial charges Q_0 and the measured recombination coefficient increases with decreasing Q_0.

$$K_r = k_{rt} + \frac{C}{Q_0} \tag{7}$$

Thus, the recombination coefficient k_r depends on the initial ion density. Therefore, only decay measurements of different analytes with equal $|Q_0|$ will be compared in the following. This allows accurate measurement of the differences in the recombination behaviour of different ion species.

To quantify the recombination coefficients of different analytes and to investigate ion–ion-recombination in gas mixtures the decay curves of the analyte peaks of ammonia, acetone and dimethyl-methylphosphonate (DMMP) at different analyte concentrations in dry clean air were analyzed. As mentioned above, $|Q_0|$ is kept constant around 5.3×10^{-14} C. Due to the high proton affinity of the used substances only positive analyte ions are formed in the ionization region. To identify their negative recombination partner, the negative ion mobility spectra were measured as well. Only negative reactant ions are present at $t_d = 11.54$ ms. Thus, all investigated positive ion species can only recombine with RIP^-. Fig. 10 shows the decay of DMMP-dimer ions. In Fig. 11 and Fig. 12 acetone-dimer ions and ammonia ions are shown. The unidentified impurities in these measurements are negligible. It is important to note, that the ion specific recombination coefficient of the analyte ion

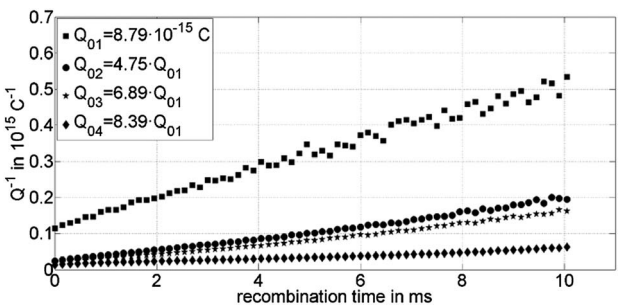

Fig. 9 $|Q(t_{rec})|^{-1}$-curves of dry clean air with different initial total charges ($|Q_{01}| = 8.79 \times 10^{-15}$ C, $|Q_{02}| = 4.75 \cdot |Q_{01}|$, $|Q_{03}| = 6.89 \cdot |Q_{01}|$, $|Q_{04}| = 8.39 \cdot |Q_{01}|$).

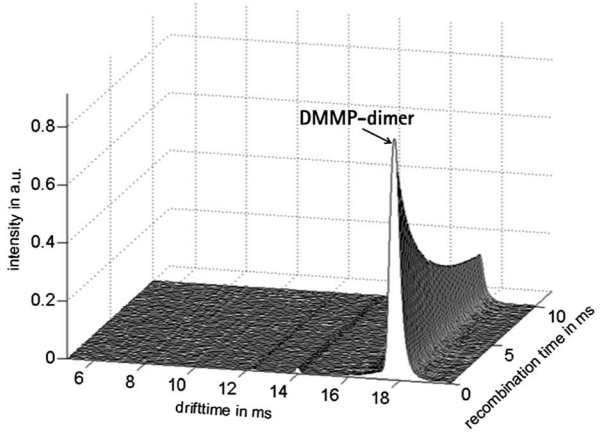

Fig. 10 Positive ion mobility spectra of dry clean air containing 200 ppb of DMMP ($t_d = 17.77$ ms) at different recombination times t_{rec}. Drift time (x-axis), recombination time (y-axis) and intensity (z-axis). Due to the high DMMP concentration mostly DMMP-dimer ions are formed. However, a small DMMP-monomer peak is visible at $t_d = 14$ ms.

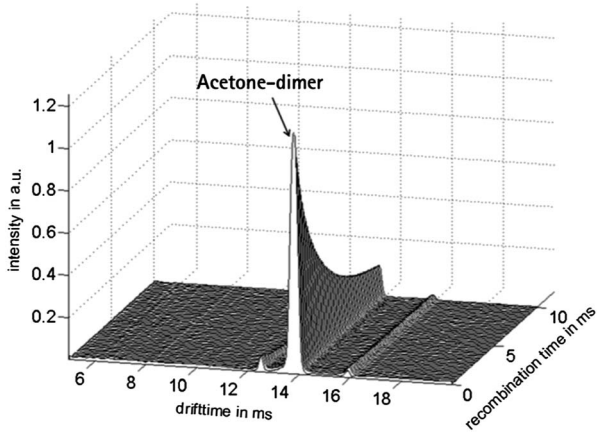

Fig. 11 Positive ion mobility spectra of dry clean air containing 7000 ppb of acetone ($t_d = 13.78$ ms) at different recombination times. The drift time (x-axis), recombination time (y-axis) and intensity (z-axis) are shown.

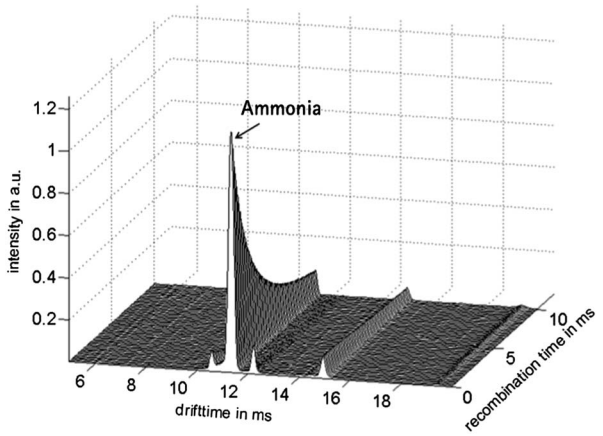

Fig. 12 Positive ion mobility spectra of dry clean air containing 122 ppb ammonia ($t_d = 11.33$ ms) at different recombination times. The drift time (x-axis), recombination time (y-axis) and intensity (z-axis) are shown.

species can be easily derived from the measurement, when only one positive analyte ion species is present in the ionization region and in the ion mobility spectrum respectively. Therefore, high analyte concentrations are used leading to single analyte peaks in the spectrum.

In Fig. 13 the ion specific $|Q(t_{rec})|^{-1}$ curves of these different ion species are compared. Here, ammonia (black filled circles) has the highest ion mobility with $K_{+,ammonia} = 2.38\ cm^2\ V^{-1}\ s^{-1}$ and the highest recombination coefficient of $2.36 \times 10^{16}\ 1\ C^{-1}\ s^{-1}$. The recombination coefficient for the acetone-dimer ions (empty circles, $K_{+,acetone} = 1.95\ cm^2\ V^{-1}\ s^{-1}$) is calculated to $2.04 \times 10^{16}\ 1\ C^{-1}\ s^{-1}$. The lowest recombination coefficient is calculated to $1.28 \times 10^{16}\ 1\ C^{-1}\ s^{-1}$ for the DMMP-dimer ions (empty squares, $K_{+,dmmp} = 1.51\ cm^2\ V^{-1}\ s^{-1}$). Thus, the higher the ion mobility the faster the recombination with negative reactant ions ($t_d = 11.54$ ms, $K_{-,RIP^-} = 2.33\ cm^2\ V^{-1}\ s^{-1}$).

Our measurements show that ion species with higher ion mobility recombine faster with the negative reactant ions than ions with lower ion mobility. Thus, one would expect that the ion–ion-recombination contains no orthogonal information on the ion mobility.

However, analyzing a mixture of 1-octanol and DMMP reveals an additional aspect besides ion–ion-recombination to be considered when interpreting decay curves of ion species. As can be seen in Fig. 14, the generated DMMP-monomer and-dimer ions have higher ion mobilities than 1-octanol-monomer, -dimer and -trimer ions. In contrast to the conclusion for single ion species from Fig. 13 – the higher the ion mobility the higher the recombination rate – 1-octanol ions decrease much faster than the DMMP monomer and dimer ions even though the ion mobilities of 1-octanol ions are lower than the ion mobilities of DMMP ions. A reasonable explanation for this observation is the significantly higher proton affinity of DMMP ($PA_{DMMP} = 902\ kJ\ mol^{-1}$) compared to 1-octanol ($PA_{1-octanol} = 846\ kJ\ mol^{-1}$) and RIP^+ ($PA_{RIP}{}^+ = 691\ kJ\ mol^{-1}$).[33,34] This leads to charge transfer reactions from positive reactant ions and 1-octanol ions to DMMP neutrals forming DMMP monomer ions and eventually stable DMMP dimer ions. As can be seen in Fig. 14, the amplitude of the DMMP-dimer ion peak increases even after stopping the electron emission. This can be explained only with charge transfer reactions and clustering in favor of stable DMMP-dimer ions.

To further characterize this behaviour, a decay measurement with dry clean air containing only 25 ppb DMMP was performed. In Fig. 15, the positive ion mobility spectra are shown.

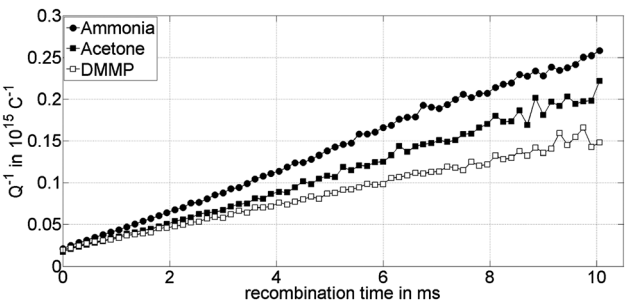

Fig. 13 $|Q(t_{rec})|^{-1}$-curve of the measured total charge of ammonia (black filled circles), acetone (black filled squares) and DMMP (empty squares).

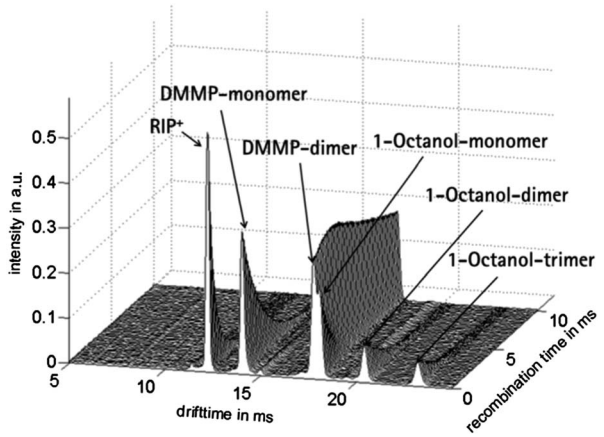

Fig. 14 Positive ion mobility spectra of dry clean air containing 25 ppb of DMMP and 19 ppb 1-octanol at different recombination times. The drift time (*x*-axis), recombination time (*y*-axis) and intensity (*z*-axis) are shown.

The detected ion species are RIP^+, DMMP-monomer and -dimer ions while only negative reactant ions were detected in the negative mode. The amplitude of the DMMP-dimer ions starts to increase after the electron gun is turned off, as already seen in Fig. 14.

To better quantify the increasing DMMP-dimer ion peak after the end of the electron emission, the peak intensities of all detected ion species are plotted *versus* t_{rec} in Fig. 16. The amplitude of the DMMP-dimer peak has a maximum at $t_{rec} = 1.5$ ms which is 8.6% higher than the initial peak amplitude. A sound explanation for the initially increasing amplitude is the formation of DMMP-monomer ions due to charge transfer from RIP^+ to DMMP neutrals and eventually stable DMMP-dimer ions due to the clustering of DMMP-monomer ions with neutral DMMP molecules. At the maximum of the DMMP-dimer peak the RIP^+ is decreased by 75%. At about this time, the DMMP-dimer formation rate becomes lower than the DMMP-dimer recombination rate. Thus, the amount of DMMP-dimer ions starts to decrease and the initial amplitude of the DMMP-dimer peak is reached again at $t_{rec} = 3$ ms.

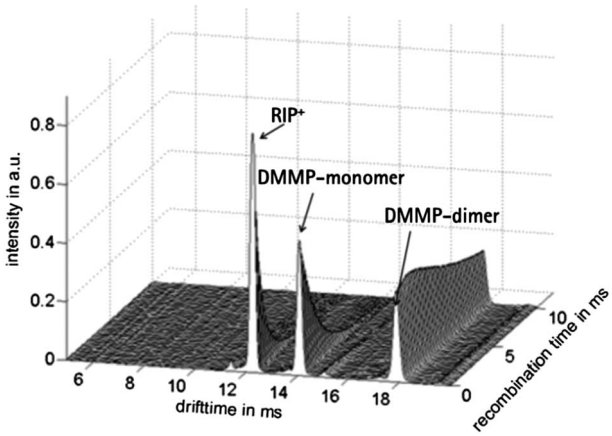

Fig. 15 Positive ion mobility spectra of dry clean air containing 25 ppb of DMMP at different recombination times. The drift time (*x*-axis), recombination time (*y*-axis) and intensity (*z*-axis) are shown.

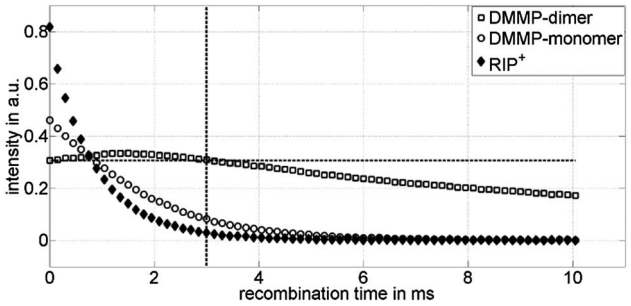

Fig. 16 Peak intensities from Fig. 15 *versus* recombination time t_{rec} of RIP^+, DMMP-monomer and -dimer ions. The RIP^+ decreases much faster than the DMMP ions. Further, the DMMP-dimer ions increase to $t_{rec} = 1.5$ ms.

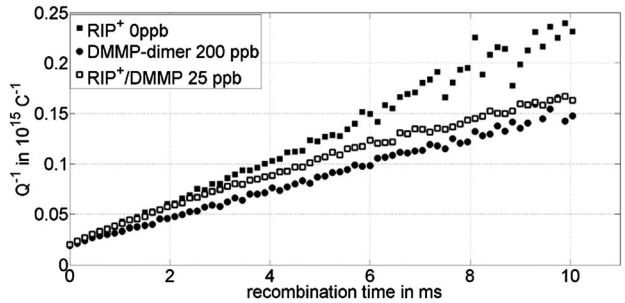

Fig. 17 Comparison of the measured total charge decay at the faraday detector between analyte concentrations of 0, 25 and 200 ppb DMMP in dry clean air.

For comparison, Fig. 17 shows the $|Q(t_{rec})|^{-1}$-curves of positive reactant ions when no other ions are present in the ionization region (Fig. 6), of DMMP-dimer ions when no other ions are present in the ionization region (Fig. 10) and a mixture of RIP^+, DMMP-monomer and -dimer ions (Fig. 15). All three measurements were performed with equal initial total charge $|Q_0|$ and dry clean air with DMMP concentrations of 0 ppb (black filled squares), 25 ppb (empty squares) and 200 ppb (black filled circles) as sample gases. As can be seen in Fig. 17, $|Q_{25ppb}(t_{rec})|^{-1}$ initially follows $|Q_{0ppb}(t_{rec})|^{-1}$ of the positive reactant ions up to a t_{rec} of 3 ms. After $t_{rec} = 3$ ms, the slopes of $|Q_{25ppb}(t_{rec})|^{-1}$ and $|Q_{200ppb}(t_{rec})|^{-1}$ become quite similar. From this we conclude, that the recombination probability of the reactant ions is higher in the presence of high proton affine substances, such as DMMP, so that in the beginning recombination of RIP^+ with RIP^- dominates the total ion loss. At t_{rec} of about 3 ms, the decay of $|Q_{25ppb}|$ is similar to the decay of $|Q_{200ppb}|$ (black circles) since RIP^+ and DMMP-monomer ions are almost disappeared. In this case only the DMMP-dimer ions can recombine with the RIP^-.

Conclusions

For the development of simple miniaturized sensors based on pulsed atmospheric pressure ionization we investigated the reaction kinetics of ion–ion-recombination in a macroscopically field-free reaction region of an ion mobility spectrometer equipped with a pulsed non-radioactive electron gun. We analyzed the ion–ion-recombination rate of several ion species such as positive and negative reactant ions, positive ammonia, dimethyl-methylphosphonate (DMMP) and acetone ions.

For all experiments we used a drift tube ion mobility spectrometer to identify and detect the different positive and negative ion species. With this setup the recombination time of the ion–ion-recombination process between the end of the electron emission, and ionization respectively, and ion injection into the drift tube can be varied.

From our experimental data we draw the following conclusions:

Since one high energetic electron generates about 600 ion pairs by atmospheric pressure ionization the concentrations of positive and negative ions in a macroscopically field-free reaction region is about $N_+ = N_-$. Furthermore, since only singly charged ions are present the measured charge $|Q|$ at the detector represents the number N of ions.

The measured ion loss caused by ion–ion-recombination matches the theoretical description:

$$\frac{1}{|Q(t_{rev})|} = \frac{1}{|Q_0|} + k_r t_{rec}$$

The recombination coefficient itself depends on the initial ion concentrations of the positive and negative ions in our experimental setup. So far, no sound explanation could be found for this dependence.

Recombination of negative reactant ions with ammonia ions, having the highest ion mobility of the compared positive ion species, is fast with the highest recombination coefficient k_r. Acetone ions with lower ion mobility recombine slower with negative reactant ions. DMMP with the lowest ion mobility has the lowest k_r when recombining with negative reactant ions.

The ion loss of specific ion species in a mixture of different ion species depends on the ion specific recombination coefficients and the proton affinities. Charge transfer from low proton affine substances to high proton affine substances can cause an initial increase in peak intensity of high proton affine substances. Furthermore, low proton affine substances dominate the initial ion loss due to an increased recombination probability. Further investigations are required to better understand ion specific losses in a mixture of different ion species.

Acknowledgements

This research is funded by the German Research Foundation (DFG).

Notes and references

1 H. Borsdorf and G. A. Eiceman, *Appl. Spectrosc. Rev.*, 2006, **41**, 323–375.
2 J. Langejuergen, P. Cochems and S. Zimmermann, *AHMT – Symposium*, 2011, pp. 199–225.
3 M. J. Cohen and F. W. Karasek, *J. Chromatogr. Sci.*, 1970, **8**, 330–337.
4 H. H. Hill Jr, W. F. Siems, R. H. St. Louis and D. G. McKinn, *Anal. Chem.*, 1990, **62**, 1201A–1209A.
5 J. I. Baumbach and G. A. Eiceman, *Appl. Spectrosc.*, 1999, **53**, 338A–355A.
6 G. A. Eiceman, A. P. Snyder and D. A. Blyth, *Int. J. Environ. Anal. Chem.*, 1990, **38**, 415–425.
7 G. A. Eiceman, *Crit. Rev. Anal. Chem.*, 1991, **22**, 471–490.

8 C. Wu, W. E. Steiner, P. S. Tornatore, L. M. Matz, W. F. Siems, D. A. Atkinson and H. H. Hill Jr, *Talanta*, 2002, **57**, 123–134.
9 W. E. Steiner, B. H. Clowers, P. E. Haigh and H. H. Hill Jr, *Anal. Chem.*, 2003, **75**, 6068–6076.
10 H. Borsdorf, T. Mayer, M. Zarejousheghani and G. A. Eiceman, *Appl. Spectrosc. Rev.*, 2011, **46**, 472–521.
11 W. E. Steiner, S. J. Klopsch, W. A. English, B. H. Clowers and H. H. Hill Jr, *Anal. Chem.*, 2005, **77**, 4792–4799.
12 D. J. Weston, R. Bateman, I. D. Wilson, T. R. Wood and C. S. Creaser, *Anal. Chem.*, 2005, **77**, 7572–7580.
13 M. A. Mäkinen, O. A. Anttalainen and M. E. T. Sillanpää, *Anal. Chem.*, 2010, **82**, 9594–9600.
14 J. E. Roehl, *Appl. Spectrosc. Rev.*, 1991, **26**, 1–57.
15 W. Vautz, D. Zimmermann, M. Hartmann, J. I. Baumbach, J. Nolte and J. Jung, *Food Addit. Contam.*, 2006, **23**, 1064–1073.
16 W. Vautz, J. I. Baumbach, M. Westhoff, K. Zóchner, E. T. H. Carstens and T. Perl, *Int. J. Ion Mobility Spectrom.*, 2010, **13**, 41–46.
17 R. G. Ewing, D. A. Atkinson, G. A. Eiceman and G. J. Ewing, *Talanta*, 2001, **54**, 515–529.
18 B. H. Clowers, P. Dwivedi, W. E. Steiner, H. H. Hill Jr and B. Bendiak, *J. Am. Soc. Mass Spectrom.*, 2005, **16**, 660–669.
19 M. R. Flannery, *Philos. Trans. R. Soc., A*, 1982, **304**, 447–497.
20 J. Langejuergen, T. Hopmeier, S. Meinen, E. Carstens, G. Theilmeier, W. Koppert and S. Zimmermann, *IMCS Proceedings*, 2012, pp. 588–591.
21 D. C. Collins and M. L. Lee, *Anal. Bioanal. Chem.*, 2002, **372**, 66–73.
22 H. E. Revercomb and E. A. Mason, *Anal. Chem.*, 1975, **47**, 970–983.
23 J. Langejuergen, *Int. J. Ion Mobility Spectrom.*, 2012, DOI: 10.1007/s12127-012-0095-z.
24 P. Cochems, F. Gunzer, J. Langejuergen, A. Heptner and S. Zimmermann, *Int. J. Ion Mobility Spectrom.*, 2011, **15**, 31–39.
25 L. B. Loeb, *Basic Process of Gasous Electronics*, Univ.of California Press, 1960.
26 S. McGowan, *Phys. Med. Biol.*, 1965, **10**, 25–40.
27 F. Gunzer, A. Ulrich and W. Baether, *Int. J. Ion Mobility Spectrom.*, 2010, **13**, 9–16.
28 A. Morozov, R. Kruecken, J. Wieser and A. Ulrich, *Eur. Phys. J. D*, 2005, **33**, 207–211.
29 A. Morozov, T. Heindl, C. Skrobol, J. Wieser, R. Kruecken and A. Ulrich, *Eur. Phys. J. D*, 2008, **48**, 383–388.
30 J. Puton, A. Knap and B. Siodłowski, *Sens. Actuators, B*, 2008, **135**, 116–121.
31 G. A. Eiceman and Z. Karpas, *Ion Mobility Spectrometry*, CRC Press, 1994.
32 H. Jungblut, *Experimental Investigation of Ion Mobility, Recombination and Charge Carrier Multiplication in Electronegative Gases*, Dissertation FU Berlin, 1981.
33 NIST Chemistry WebBook, http://webbook.nist.gov/chemistry/.
34 M. Tabrizchi and S. Shooshtari, *J. Chem. Therm.*, 2003, **35**, 863–870.

